Biomaterials 103 (2016) 75–85

Contents lists available at ScienceDirect

Biomaterials

journal homepage: www.elsevier.com/locate/biomaterials

Fullerene/photosensitizer nanovesicles as highly efficient and clearable phototheranostics with enhanced tumor accumulation for cancer therapy

Mirong Guan [a], Jiechao Ge [b, **], Jingyi Wu [a], Guoqiang Zhang [a], Daiqin Chen [a], Wei Zhang [a], Ying Zhang [a], Toujun Zou [a], Mingming Zhen [a], Chunru Wang [a], Taiwei Chu [c], Xiaojuan Hao [d], Chunying Shu [a, *]

[a] Key Laboratory of Molecular Nanostructure and Nanotechnology, Institute of Chemistry, Chinese Academy of Sciences, Beijing National Laboratory for Molecular Sciences, Beijing 100190, China
[b] Key Laboratory of Photochemical Conversion and Optoelectronic Materials, Technical Institute of Physics and Chemistry (TIPC), Chinese Academy of Sciences, Beijing 100190, China
[c] Department of Applied Chemistry, College of Chemistry and Molecular Engineering, Peking University, Beijing 100871, China
[d] Manufacturing Flagship, Commonwealth Scientific and Industrial Research Organization (CSIRO), Clayton, VIC 3168, Australia

ARTICLE INFO

Article history:
Received 6 April 2016
Received in revised form
9 June 2016
Accepted 10 June 2016
Available online 21 June 2016

Keywords:
Nanovesicle
Fullerene
Photosensitizer
Phototheranostic

ABSTRACT

A novel phototheranostic platform based on *tri*-malonate derivative of fullerene C_{70} (TFC_{70})/photosensitizer (Chlorin e6, Ce6) nanovesicles (FCNVs) has been developed for effective tumor imaging and treatment. The FCNVs were prepared from amphiphilic TFC_{70}-oligo ethylene glycol -Ce6 molecules. The developed FCNVs possessed the following advantages: (i) high loading efficiency of Ce6 (up to ~57 wt%); (ii) efficient absorption in near-infrared light region; (iii) enhanced cellular uptake efficiency of Ce6 *in vitro* and *in vivo*; (iv) good biocompatibility and total clearance out from the body. These unique properties suggest that the as-prepared FCNVs could be applied as an ideal theranostic agent for simultaneous imaging and photodynamic therapy of tumor. This finding may provide a good solution to highly efficient phototheranostic applications based on fullerene derivatives fabricated nanostructures.

1. Introduction

Phototheranostics, which refers to diagnosis *via* application of light with simultaneous treatment of disease, has emerged as a promising interdisciplinary technique for imaging guided tumor treatment due to improvement in light generation, delivery, and sensing technologies [1–5]. Among phototheranostics, photodynamic therapy (PDT) based theranostics as an alternative tumor-ablative method has unique advantage in comparison with the conventional methods (i.e. surgery, chemotherapy and radiotherapy) since it is a less invasive and more controllable technique, which has been approved by Food and Drug Administration for treatment of various non-malignancies and malignancies [6,7]. In PDT, photosensitizer (PS) as a key component could transfer the energy of light to surrounding oxygen [8–10], producing reactive oxygen species (ROS) to induce irreversible damage of cancer cells and achieve an effective tumor ablation [11–13]. Chlorin e6 (Ce6) as a most commonly used PS, has stronger absorption in near-infrared (NIR) light region and higher singlet oxygen ($^1O_2$) quantum yield because of its large π-conjugated aromatic domains [14,15]. Moreover, Ce6 could be further used as a NIR fluorescence (FL) imaging agent in the spectral range of 650–800 nm to avoid the interference of endogenous chromophores within the body [16]. However, Ce6 is highly insoluble in water and tends to form aggregates, as a result, reducing its PDT efficiency due to the π-π interactions [17]. Moreover, Ce6 as a small molecule usually exhibits non-specific delivery and non-ideal biodistribution properties and therefore hardly meets the requirement of real-time tumor treatment [18].

As smart carbonaceous nanomaterials, fullerene derivatives have been reported as PSs for PDT due to their good biocompatibility, facile multiple surface functionalization, and efficient

* Corresponding author.
** Corresponding author.
E-mail addresses: jchge2010@mail.ipc.ac.cn (J. Ge), shucy@iccas.ac.cn (C. Shu).

http://dx.doi.org/10.1016/j.biomaterials.2016.06.023

generation of ROS even under lower oxygen conditions [19–23]. Most importantly, fullerene derivatives could be totally cleared out from the body according to the reports in literature [24–26]. Unfortunately, the UV-to-Vis excitation of fullerene derivatives hinders the enhancement of PDT efficiency *in vivo* due to the limited penetration depth of UV-to-Vis irradiation [27–32].

The application of self-assembled nanomaterials for PDT has the potential to overcome these aforementioned limitations of Ce6 and fullerene derivatives by enabling the engineered nanostructures to navigate *in vivo* in specific ways and enhancing the NIR light absorption of fullerene [33,34]. As we know, amphiphilic molecule is widely used to self-assemble into nanovesicles through the controlled balance between hydrophilic parts and hydrophobic parts [35–37]. The formed nanovesicles have attracted considerable attention due to their hollow structures similar to the organelles in cells as well as their emerging collective properties arising from coupling between nanoparticles within assemblies [38–43]. Currently, numerous amphiphilic materials such as chitosan, polymer, liposome, protein, and gold nanoparticles, have been reported to self-assemble into vesicles for drug delivery and cancer therapy [44–51]. However, so far there is no report about the nanovesicles based on amphiphilic fullerene derivatives for phototheranostics application. Therefore, it is of great interest to develop nanovesicles based on fullerene derivatives/PS and explore their cancer therapy efficiency as novel phototheranostic agents.

Herein, we report a new phototheranostic platform based on *tri*-malonate derivative of fullerene (TFC_{70})/PS (Ce6) nanovesicles (FCNVs), and 1,10-Diamino-4,7-dioxadecane (OEG2) as a linker, as shown in Scheme 1. Amphiphilic TFC_{70}-OEG2-Ce6 molecule was prepared *via* coupling reaction between amine groups on OEG2 modified Ce6 and carboxylic groups on TFC_{70} in water/DMSO mixture solution. We then dialyzed the as-prepared amphiphilic molecules to form the water-dispersible FCNVs. The obtained water-dispersible and biocompatible FCNVs, not only could carry a large amount of Ce6 to tumour site for imaging-guided and NIR light-triggered PDT treatment, but also could excrete from body after PDT. As far as we know, this study is the first to demonstrate the preparation of FCNVs as phototheranostics for imaging-guided efficient PDT *in vivo*, which may provide a new strategy for efficient phototheranostic applications based on fullerene derivatives fabricated nanostructures.

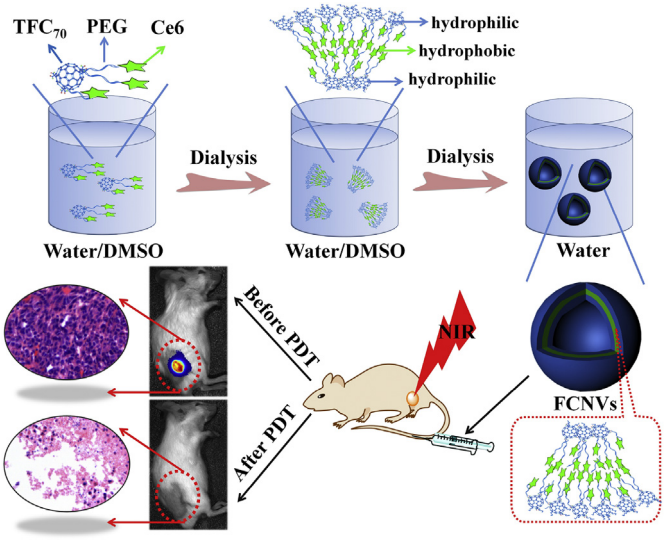

Scheme 1. Schematic fabrication of FCNVs as phototheranostic agent for PDT.

2. Experimental section

2.1. Materials

Chlorin e6 was purchased from Innochem. 1,8-Diamino-3,6-dioxaoctane, 1-(3-Dimethylaminopropyl)-3-ethylcarbodiimide hydrochloride (EDC), N-Hydroxysuccinimide (NHS), Di-*tert*-butyl pyrocarbonate ($(Boc)_2O$), 1,8-diazobicyclo[5,40]undec-7-ene (DBU) and trifluoroacetic acid (TFA) were purchased from Acros. The culture medium Dulbecco's modified Eagle's medium (DMEM) (Invitrogen, USA) supplemented with 10% fetal bovine serum (FBS, Hyclone Company, South Logan, UT), penicillin (100 μg mL^{-1}), and streptomycin (100 μg mL^{-1}) (Gibco, Grand Island, N. Y. USA), Cell counting Kit-8 (CCK-8; DOJINDO, Kumamoto, Japan), Dil, MitoRed, Lyso, PI and Hoechst 33258 were purchased from PuJingKangLi. All other chemicals used were analytical reagents.

2.2. Characterization

^1H NMR spectroscopy was recorded on Bruker Advance 400 MHz NMR spectrometer at 25 °C. Matrix-assisted laser desorption/ionization time of flight mass spectra (MALDI-TOF MS) were measured though AXIMA Assurance MALDI-TOF system. The particle sizes and Zeta potentials were determined by dynamic light scattering (DLS) using Malvern Nano-ZS90 apparatus (Malvern Instruments). Scanning electron microscopy (SEM) was carried out on a JEOL JSM-6701F electron microscope, Transmission electron microscopy (TEM) was carried out on JEOL-JEM 2100F field emission transmission electron microscope at 200 kV, and Atomic force microscopy (AFM) was carried on MultiMode 8 (Bruker) were used to characterize the morphology of FCNVs. Absorbance measurements were carried out using UV2550 spectrophotometer (SHIMADZU). FL spectra were acquired though Fluorolog spectrophotometer. Fourier transform infrared spectroscopy (FTIR) spectra were measured using Thermo instrument (NICOLET IN10 MX). Flow cytometric analysis was performed on flow cytometer (ACCURIC6). Cell viability was detected by 96-well plate reader (iMarkmicroplate reader, Bio-RAD, USA).

2.3. Synthesis of Boc-OEG2

The OEG2 (1 equiv.) in dichloromethane (DCM) solution was treated with Boc_2O (0.15 equiv.) in default for 5 h at 0 °C and then stirred at room temperature for 18 h. The organic phase was washed with water until all the unreacted OEG2 was extracted. The Boc-protected OEG2 was evaporated under vacuum after drying with $MgSO_4$. ^1H NMR spectroscopy was used to confirm the structure of Boc-OEG2 (Fig. S1†). ^1H NMR (400 MHz, $CDCl_3$, 298 K) δ = 5.26 (s, 1H, NHBoc), 3.51–3.44 (m, 4H, 2 × glycol CH_2), 3.43–3.39 (m, 4H, 2 × glycol CH_2), 3.20–3.18 (m, 2H, CH_2NHBoc), 2.78–2.75 (t, J = 5.6 Hz, 2H, CH_2NH_2), 1.87 (broad s, 2H, NH_2), 1.33 (s, 9H, CH_3).

2.4. Synthesis of Ce6-OEG2-Boc

100.0 mg (0.167 mmoL) of Ce6 was dissolved in 30 mL of DMSO. 58.0 mg (0.30 mmoL) of EDC and 26.5 mg (0.23 mmoL) of NHS were added into the above solution and stirred at room temperature for 1 h. Then 33.3 mg (0.13 mmoL) of Boc-OEG2 in 10 mL of DMSO was added to above solution following by vigorously stirring for 24 h. After that, the crude products were washed with water to remove excess NHS and EDC. Then crude products were separated and purified by silica gel chromatography with DCM: EtOH (v:v = 9:1) to afford Ce6-OEG2-Boc as confirmed by MALDI-TOF-MS (Fig. S2†).

2.5. Synthesis of Ce6-OEG2

TFA (25%) in DCM was added to Ce6-OEG2-Boc, which was stirred at 0 °C for 2 h to remove the *tert*-butyl group. After that, solvent was evaporated under vacuum and the crude product was dissolved in ethyl acetate. The pH of solution was adjusted to 8–9 by 5% sodium carbonate. Then solvent was evaporated and the product was confirmed by MALDI-TOF-MS (Fig. S3†).

2.6. Synthesis of tri-malonic acid modified fullerene (TFC_{70})

Malonic acid fullerene derivative was prepared according to our previously reported [52]. Briefly, C_{70} was converted into fullerene malonic ester by treatment with diethyl bromomalonate and DBU in dry toluene under nitrogen. The *tri*-malonate derivative of fullerene was separated by silica gel column chromatography and characterized by MALDI-TOF-MS. Hydrolysis of the purified malonic acid fullerene derivative with NaH and CH_3OH led to the formation of the corresponding acid (TFC_{70}).

2.7. Synthesis of FCNVs

TFC_{70} (21.8 mg, 0.02 mmoL) was dissolved in water (30 mL). 44.0 mg (0.23 mmoL) of EDC and 20.0 mg (0.17 mmoL) of NHS were added into the above solution and stirred at room temperature for 1 h. Then 100.0 mg (0.12 mmoL) of Ce6-OEG2 in 10 mL of DMSO was added to above solution following by vigorously stirring for 24 h. The crude product was dialyzed against water for one week and characterized by MALDI-TOF-MS (Fig. S4†), FTIR (Fig. S5†), SEM & TEM (Fig. 1), UV–Vis spectrophotometry and DLS (Fig. 2).

2.8. Density functional theory (DFT) calculations

DFT calculations were preformed to estimate the molecular length by using the Dmol [3] code, all the calculations are represented at the double-numeric quality basis set with double numerical plus polarization (DNP) functions level, which are comparable to Gaussian 6-31G** sets. The exchange correlation interactions are described by the Perdew–Burke–Ernzerhof generalized gradient approximation (GGA). All atomic positions are fully relaxed at the GGA level without symmetry restriction until the atomic forces are smaller than 10^{-5} Hartree.

2.9. Ce6 loading efficiency measurements

To estimate the loading efficiency of Ce6 on TFC_{70}, FCNVs powder was collected by vacuum drying which was quantified by using UV calibration curve of Ce6 at 403 nm. And the conjugated Ce6 amount could be calculated by the equation: Ce6 loading efficiency = (weight of Ce6)/(weight of Ce6 + weight of TFC_{70}). Every experiment was repeated three times. In the calibration curve, the absorption intensity of 403 nm is linearly proportional to the concentration of Ce6, following a regression equation: $Y = 0.0132 + 1.1846X$ ($R^2 = 0.9997$). This is reasonably consistent with the MALDI-TOF MS of FCNVs (Fig. S4†).

2.10. In vitro cytotoxicity of FCNVs

The cytotoxicity of A549 cells toward FCNVs *in vitro* was carried out. A549 cells were seeded in a 96-well plate with a density of ca. 5×10^4 per well and cultured in 5% CO_2 at 37 °C for 24 h. A549 cells were then treated with a series of gradient concentration of FCNVs for 3 h in the dark and then irradiated with a 660 nm laser for 10 min (20 mW cm^{-2}). A549 cells only treated with FCNVs in the dark for 24 h were used as a control. Then the culture medium was replaced and the cells were cultivated for another 24 h in the dark at 37 °C. Cytotoxicity was evaluated by using a WST-8 assay with CCK-8 which has characteristic absorbance at 450 nm. This can be read with a 96-well plate reader to determine the cell viability. A549 cells treated with either FCNVs (0.2 mg mL^{-1}), or TFC_{70} (0.1 mg mL^{-1}), and Ce6 (0.1 mg mL^{-1}) respectively, and blank cells were used as controls. Both the Ce6 effective concentration of FCNVs and Ce6 alone are 0.1 mg mL^{-1}. Then the cell viabilities were detected by using CCK-8. Results are expressed as means ± SD.

2.11. Confocal images of treated A549 cells after stained with Hoechst 33258, PI, Dil, MitoRed and LysoBlue

A549 cells were incubated with FCNVs (0.2 mg mL^{-1}) at 37 °C, 5% CO_2 for 3 h, then the aged cell culture was replaced with fresh DMEM (without phenol red), the cells were exposed to an external 660 nm (20 mW cm^{-2}) laser for 10 min. After that either Hoechst 33258 (1 mg mL^{-1}, 5 μL, incubated with cell for 20 min), or PI (1 mg mL^{-1}, 5 μL, incubated with cell for 15 min), Dil (1 mg mL^{-1}, 5 μL, incubated with cell for 20 min), MitoRed (1 mg mL^{-1}, 5 μL, incubated with cell for 30 min) and Lyso (1 mg mL^{-1}, 5 μL, incubated with cell for 45 min) were added respectively according to the actual conditions and washed with icy PBS buffer for three times before observation. The images were obtained by FV 1000-IX81 confocal laser scanning microscope (Olympus, Japan). The cells dyed under the same conditions without laser irradiation were used as controls.

2.12. Animal experiments

Female Balb/c mice (16–20 g) were purchased from Center for Experimental Animals, Institute of Process Engineering, Chinese Academy of Science (Beijing, China). *In vivo* study conforms to the guidelines of the National Regulation of China for Care and Use of Laboratory Animals. The tumor model was established by subcutaneous injection of 4T1-*luc* cells in the right buttock of each mouse. The tumors were allowed to grow for 5 days to reach the size of around ca. 50–100 mm^3.

2.13. In vivo fluorescence imaging (FL)

FL imaging was performed on an *in vivo* imaging system (CRI Maestro 2) with a 660 nm laser as the light source. The FL imaging were collected at 560–800 nm and analyzed with Maestro2 software. The Balb/c mice were anesthetized with 1.5% pentobarbital sodium by intraperitoneal injection at a dose of 120 μL. FCNVs (1 mg mL^{-1}, 200 μL) were injected by intravenous injection and the FL imaging was performed at timed intervals (0, 1, 4, 24 and 48 h). Ce6 (0.5 mg mL^{-1}, 200 μL) was injected as control group. Both the Ce6 effective concentration of FCNVs and Ce6 alone are 0.5 mg mL^{-1}.

2.14. In vivo toxicity studies

The tumor-bearing mice were randomized into four groups (n = 5, each group). Group 1 was treated by intravenous injection with FCNVs at a dose of 200 μL (1 mg mL^{-1}), after 4 h post-injection, tumor site was irradiated with 660 nm laser for 10 min (100 mW cm^{-2}). Group 2 was treated with saline (200 μL) and irradiated with 660 nm laser for 10 min (100 mW cm^{-2}). Another two groups treated with either FCNVs (1 mg mL^{-1}, 200 μL) or saline (200 μL) only without laser irradiation were also used as controls. All the groups were received only once injection. The body weights and tumor volumes were monitored every two days after treatment. The tumor volume was calculated using the following

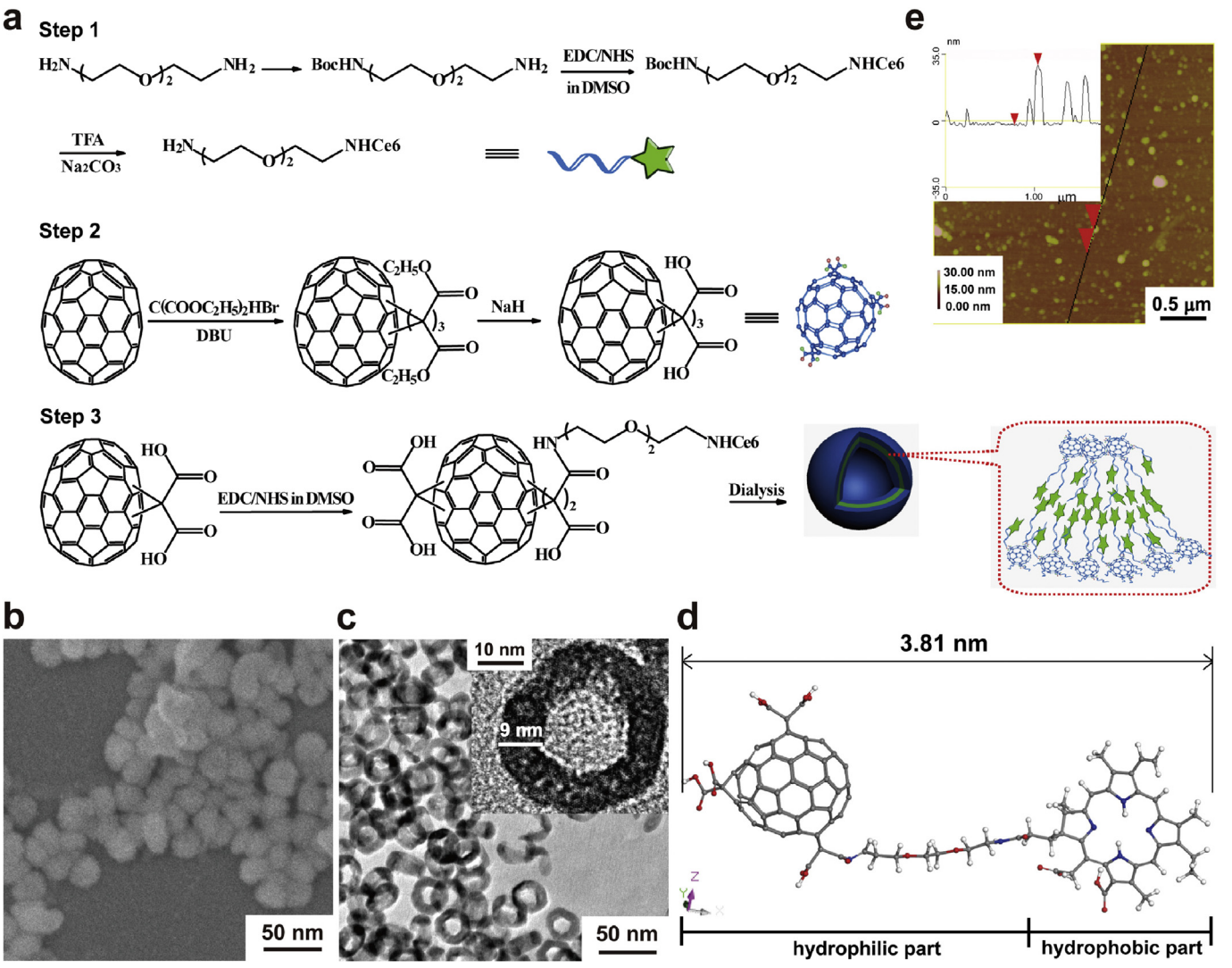

Fig. 1. (a) Illustration of the synthesis of FCNVs; (b) SEM image of FCNVs; (c) TEM image of FCNVs; (d) Optimized structure of TFC_{70}/Ce6-OEG2 at the GGA-PBE/DNP theoretical level by the DFT; (e) AFM image of FCNVs and the height of FCNVs is ca. 32 nm.

equation: tumor volume (V) = length × width [2]/2. Relative tumor volume was calculated as V/V_0 (V_0 is the corresponding tumor volume when the treatment was initiated).

2.15. ^{131}I labeling of FCNVs

$Na^{131}I$ was obtained from Peking University, FCNVs were labeled by ^{131}I using a standard chloramine T oxidation method [53]. A mixture of 2 mL of FCNVs (2 mg mL^{-1}), 2.0 MBq $Na^{131}I$ and 100 μL chloramine-T (10 mg mL^{-1}, Sigma-Aldrich) were reacted in a pH 7.5 phosphate buffer (0.02 M) for 2 h at room temperature. Excess ^{131}I was separated by silica gel column chromatography, and then washed by centrifugal filtration through Amicon filters (MWCO = 3 kDa) and washed with water 4–6 times until no gamma activity was detected in the filtrate solution. A radiolabeling yield of 46% (purity ≥97%) was achieved.

2.16. Biodistribution

Female Balb/c mice (Harlan, USA) were injected with the solution of ^{131}I-FCNVs in saline (6–7 μCi, 200 μL) *via* the tail vein. The body weight of the animals used in this study averaged ca. 20 g. The mice were sacrificed and blood samples and major organs were collected at assigned time points after injection (1 h, 4 h, 24 h, 2 d, 7 d, 15 d, and 20 d; n = 5 per time point). The radioactivity of each sample was measured by gamma counting. The percent of injected dose per gram (%ID per g) of tissues was calculated from gamma counting.

2.17. Bioluminescence imaging in vivo

Bioluminescence imaging was performed with a CALIPER Lumina II *in vivo* imaging system (IVIS). A 680-sp filter was employed as the emission filter for *in vivo* imaging tests and the exposure time is 0.3 s. The tumor-bearing Balb/c mice were anesthetized with 1.5% pentobarbital sodium by intraperitoneal injection at a dose of 120 μL. D-Luciferin potassium (15 mg mL^{-1}, 200 μL) was injected by intraperitoneal injection and the bioluminescence imaging was performed before and after PDT treatment for 15 days.

2.18. Histopathological examination

The major tissues (heart, liver, spleen, kidneys, and lung) were harvested and fixed in a 4% formalin solution. The histopathological

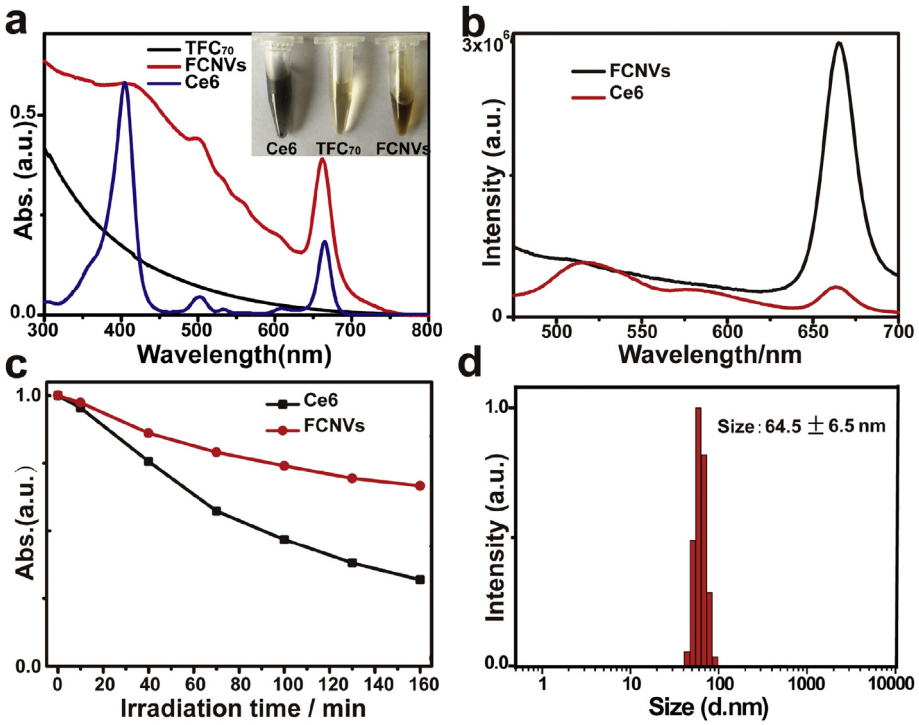

Fig. 2. (a) UV–Vis absorption spectra of FCNVs (0.65 μg mL^{-1}, in water), Ce6 (0.30 μg mL^{-1}, in DMSO) and TFC$_{70}$ (0.29 μg mL^{-1}, in water). Both the concentrations of Ce6 in FCNVs and pristine Ce6 are 0.30 μg mL^{-1}, and both of the concentrations of TFC$_{70}$ in FCNVs and pristine TFC$_{70}$ are 0.29 μg mL^{-1}. Inset is photographs of Ce6, TFC$_{70}$ and FCNVs aqueous solution; (b) FL spectra of FCNVs (in water) and Ce6 (in water). Both the concentrations of Ce6 in FCNVs and pristine Ce6 are 0.1 mg mL^{-1}; (c) The relative UV–Vis absorption of FCNVs and Ce6 exposed to light irradiation for 10, 40, 70, 100, 130, 160 min, respectively, at a power density of 50 mW cm^{-2}; (d) Size distribution of FCNVs measured in water.

tests were performed according to standard laboratory procedures. Tissue samples were numbered and given blind to the pathologist for conventional processing and analysis. Briefly, the tissue samples were embedded in paraffin blocks, sectioned into 4 μm slices, and mounted onto the glass slides. After hematoxylin eosin (H&E) staining, the sections were observed, and photographs were taken using an optical microscope.

2.19. Statistical analysis

The statistical analysis of the samples was conducted by Student's *t*-test, $p < 0.01$ were very significant (**). All data reported are means ± standard deviations, unless otherwise noted.

3. Results and discussion

3.1. Preparation and characterization of FCNVs

In order to facilitate the successful coupling of Ce6 and TFC$_{70}$, OEG2 was introduced to Ce6, as shown in Fig. 1a (step 1) [54]. The chemical structure of Boc-OEG2 was confirmed by ^{1}H NMR [55] (Fig. S1†). Then, Ce6 was covalently linked with Boc-OEG2, the molecular weight of obtained Ce6-OEG2-Boc was measured by MALDI-TOF MS to be 826 (Fig. S2†), which is consistent with its theoretical value. Finally, TFA was used to remove Boc-group, Ce6-OEG2 with molecular weight of 726 (Fig. S3†) was obtained. The involvement of smart OEG2 linkers facilitates the coupling reaction of Ce6 and TFC$_{70}$. The OEG2 linker prevents the direct interaction between Ce6 and TFC$_{70}$, preserving the fluorescence of Ce6 to some extent. Furthermore, the smart OEG2 also could minimize the nonspecific interaction between obtained FCNVs and biological molecules [54,56].

The FCNVs were prepared as illustrated in Fig. 1a (Steps 2–3). In step 2, fullerene (C$_{70}$) was initially modified with malonic acid as TFC$_{70}$, according to the previously reported [52]. In brief, C$_{70}$ was converted into fullerene malonic ester following treatment with diethyl bromomalonate in dry toluene under nitrogen. The *tri*-malonate derivative of C$_{70}$ was separated by silica gel column chromatography. Hydrolysis of the purified products with NaH and CH_3OH led to the formation of TFC$_{70}$. After that, in step 3, TFC$_{70}$ was covalently linked with Ce6-OEG$_2$ in water/DMSO mixture solution (*v*/*v*, 4:1) to obtain Ce6-OEG2/TFC$_{70}$. The obtained Ce6-OEG2/TFC$_{70}$ was measured in methanol by MALDI-TOF MS to be 2576 (2526 + 14) and 2590 (2526 + 28) (Fig. S4†), which exceeded its theoretical value (2526) by one or two methylene, due to the involvement of methanol. The FTIR spectra in Fig. S5† exhibited characteristic vibration of amide bond at 3370 cm^{-1}, 1645 cm^{-1}, and 1400 cm^{-1}, indicating the successful preparation of amphiphilic molecule, TFC$_{70}$/Ce6-OEG2, in which TFC$_{70}$-OEG2 acts as hydrophilic part and Ce6 as hydrophobic part. The amphiphilic properties enable TFC$_{70}$/Ce6-OEG2 self-assemble into vesicular structures through balance between two competing interactions during the dialysis process in water [57–59].

SEM image (Fig. 1b) reveals that the morphology of the resulting FCNVs is spherical with an average size of ca. 31 nm. TEM image in Fig. 1c suggests that the individual FCNVs are hollow spheres with shell thickness of ca. 9 nm. For better understanding of the resulting structure, the molecular length of TFC$_{70}$/Ce6-OEG2 is optimized at the GGA-PBE/DNP theoretical level by the DFT [60] to be ca. 3.81 nm (Fig. 1d), which is approximately half that of the shell thickness of FCNVs, suggesting that bilayer nanovesicles are formed. The height of the FCNVs measured from AFM is about 32 nm (Fig. 1e), which is in a well agreement with SEM/TEM results and further confirms the formation of nanovesicles, whereas the height of TFC$_{70}$ in AFM image is about 2 nm (Fig. S6†).

The UV–Vis spectra illustrate that FCNVs exhibit a stronger

absorption at ca. 660 nm than that of free Ce6, indicating the assembled structure can enhance the absorption (Fig. 2a). The FL emission spectra of Ce6 and FCNVs exhibit the similar emissive peak around 660 nm, as shown in Fig. 2b, the FL intensity of FCNVs in aqueous solution is higher than that of free Ce6 due to the poor solubility of Ce6 in water [61]. To investigate the interactions between TFC_{70} and Ce6, the FL emission spectra of Ce6, TFC_{70}/Ce6-OEG2, and FCNVs in water-DMSO mixture solution (*v*/*v*, 95/5) were further investigated. As shown in Fig. S7†, partial FL emission of Ce6 is quenched in both FCNVs and TFC_{70}/Ce6-OEG2, due to the partial close proximity of Ce6 to TFC_{70}. The FL intensity of FCNVs is lower than that of TFC_{70}/Ce6-OEG2 which may ascribe to the π-π stacking interaction between Ce6 molecules in FCNVs, similar to the previous studies on the Ce6 based nanostructures for PDT [16,62].

The time-dependent photostability of FCNVs was investigated under an irradiation of 660 nm (50 mW cm^{-2}). As shown in Fig. 2c, the absorbance intensity of FCNVs decreases slowly while that of Ce6 decreases rapidly, indicating FCNVs possess improved photostability. This phenomenon may ascribe to the energy transfer between C_{70} and Ce6, which result in the unique physical and chemical properties of Ce6 [16,62]. FCNVs are stable in FBS as shown in Fig. S8†, which would facilitate its biomedical application. The DLS investigation shows that the diameters of FCNVs are ca. 65 nm in aqueous solution (Fig. 2d), ca. 103 nm in FBS and ca. 120 nm in PBS, respectively (Fig. S9†). This obvious difference should ascribe to the different media. As literature reported, serum proteins once associated with negative and positive charged nanoparticles would form protein corona, leading to the increase of size of nanoparticles in FBS [63]. Furthermore, the increased size of FCNVs in PBS should benefit from the change of surface potential [13,64]. This size distribution could enable FCNVs to specifically accumulate in tumour site through enhanced permeability and retention (EPR) effect [65]. The Zeta potential of FCNVs is approximately − 25.6 mV in water, indicating the surface of FCNVs is negative charged (Fig. S10†). Ce6 loading efficiency on TFC_{70} could be quantified by using the UV–Vis calibration curve of Ce6 at 403 nm (Fig. S11†) [16]. Notably, the maximum loading efficiency can reach to ~57 wt%, which is much higher than those previously reports where Ce6 was loaded through either encapsulation or π-π interaction (Table 1) [14,16,54,66–69]. This is further confirmed by MALDI-TOF MS (Fig. S4†).

3.2. In vitro imaging and PDT

To investigate PDT effect of FCNVs, the capability of cell uptake was initially studied. A549 cells were incubated with either FCNVs or free Ce6 (at an equiv. Ce6 dose of 0.1 mg mL^{-1}) for 0.5, 1, 3, 7 and 24 h at 37 °C and then imaged by a confocal FL microscope. As shown in Fig. 3a, although the intracellular FL increased over time for both Ce6 and FCNVs incubated cells, the latter showed much stronger FL. Furthermore, quantitative evaluation of the cellular uptake toward Ce6 and FCNVs was carried out by comparing the FL intensities of cellular lysates at different incubation time (0.5, 1, 3, 7 and 24 h). As revealed by Fig. 3b, the FL of FCNVs treated cells is much higher than that of free Ce6, indicating the enhanced cellular uptake of FCNVs, due to their good water-dispersibility and vesicular structure, which is similar with previous report [70]. To validate the concomitant generation of ROS induced by FCNVs under 660 laser irradiation, 2′,7′-dichlorofluorescein diacetate (DCFDA) [71], a standard FL indicator for ROS was initially used to stain A549 cells. As shown in Fig. 3c and d, the cells exposed to FCNVs and Ce6 show intensifying FL of DCFDA over irradiation time, clearly indicating the production of ROS. Notably, FL of DCFDA from FCNVs treated cells is much higher than that of free Ce6, whereas cells treated with DCFDA alone exhibit negligible FL, indicating the enhanced ROS generation of FCNVs [72]. Free radical species detection was subsequently carried out to identify which kind of ROS was produced by FCNVs upon laser irradiation with different ROS scavengers [20]. A549 cells were incubated with FCNVs (0.2 mg mL^{-1}) in the dark for 3 h first, and then the medium was replaced by DMEM without phenol red, containing either 10 mM sodium azide (NaN_3), mannitol, or SOD (50 units). Subsequently, the cells were irradiated at 660 nm laser for 10 min. From the results shown in Fig. S12†, we found that FCNVs alone efficiently produced photo-damage toward cells while the $^1O_2$ quencher (NaN_3) intensively blocked the FCNVs-induced cell death. In contrast, the added free radical inhibitors (mannitol and SOD) did not protect cells from FCNVs-induced photo-damage. The results clearly demonstrate that FCNVs-induced cell death benefits from the generation of $^1O_2$. Furthermore, the $^1O_2$ production of FCNVs and Ce6 were measured by using electron spin resonance (ESR) spectroscopy under the same dose of Ce6. As shown in Fig. S13†, the $^1O_2$ production of FCNVs is higher than that of free Ce6 under the same conditions, which may benefit from the stronger absorption of FCNVs at ca. 660 nm [16,40].

To the PDT effect of FCNVs, the *in vitro* viability assay of A549 cells were selected as model. As shown in Fig. 3e, negligible cytotoxicity is observed when A549 cells are incubated with FCNVs at a series of gradient concentrations up to 0.2 mg mL^{-1} in the dark, indicating the favorable biocompatibility of FCNVs. In contrast, the cell viabilities decrease significantly with increasing FCNVs concentration upon 660 nm laser irradiation at power density of 20 mW cm^{-2} for 10 min, and 95% inhibitory effect is achieved at 0.2 mg mL^{-1} of FCNVs. In order to show the excellent PDT efficiency of FCNVs, we compare the cell viabilities treated by FCNVs with that of free Ce6 (at an equiv. Ce6 dose of 0.1 mg mL^{-1}) or TFC_{70} alone (0.1 mg mL^{-1}) under the same conditions (Fig. 3f). The results indicate that FCNVs exhibited a much better PDT efficiency than either free Ce6 or TFC_{70} alone. The reasons on one hand may ascribe to the higher uptake of FCNVs with a high coupling efficiency of Ce6 by A549 cells than that of free Ce6, on the other hand, should benefit from the highly efficient absorption of FCNVs at 660 nm than that of free TFC_{70} [16,40]. Furthermore, human immortal keratinocyte line (HaCaT) was used as a control to explore the selectivity of FCNVs and Ce6. As shown in Fig. S14†, either FCNVs or Ce6 shows a favorable lethality to A549 cells under laser irradiation, which may contribute to the higher uptake of FCNVs or Ce6 to cancer cells than normal cells (Fig. S15†) [20].

In addition, confocal images (Fig. S16†) were recorded to investigate the dynamic process of cell death by observing the bubble produced by the cells under light irradiation. At the same time, red FL emitted from FCNVs could be detected in cytoplasm which indicated that FCNVs were uptaken into cytoplasm of cells. Several subcellular organelles were stained by related probes and observed under confocal microscope to confirm that the cells were destructed after incubation with FCNVs followed by subsequent

Table 1
Loading efficiency of Ce6 with different nanomaterials.

Nanocarriers	Drug loading efficiency (wt%)
FCNVs	57
Iron oxide nanoclusters	6.5[14]
Gold nanoparticles	18.4[16]
Fullerene (C_{60}) derivatives	23–26[54]
Silica-coated-gold nanoclusters	14.6[66]
Graphene oxide	15[67]
Upconversion nanoparticles	6–8[68]
MoS_2 nanosheets	30[69]

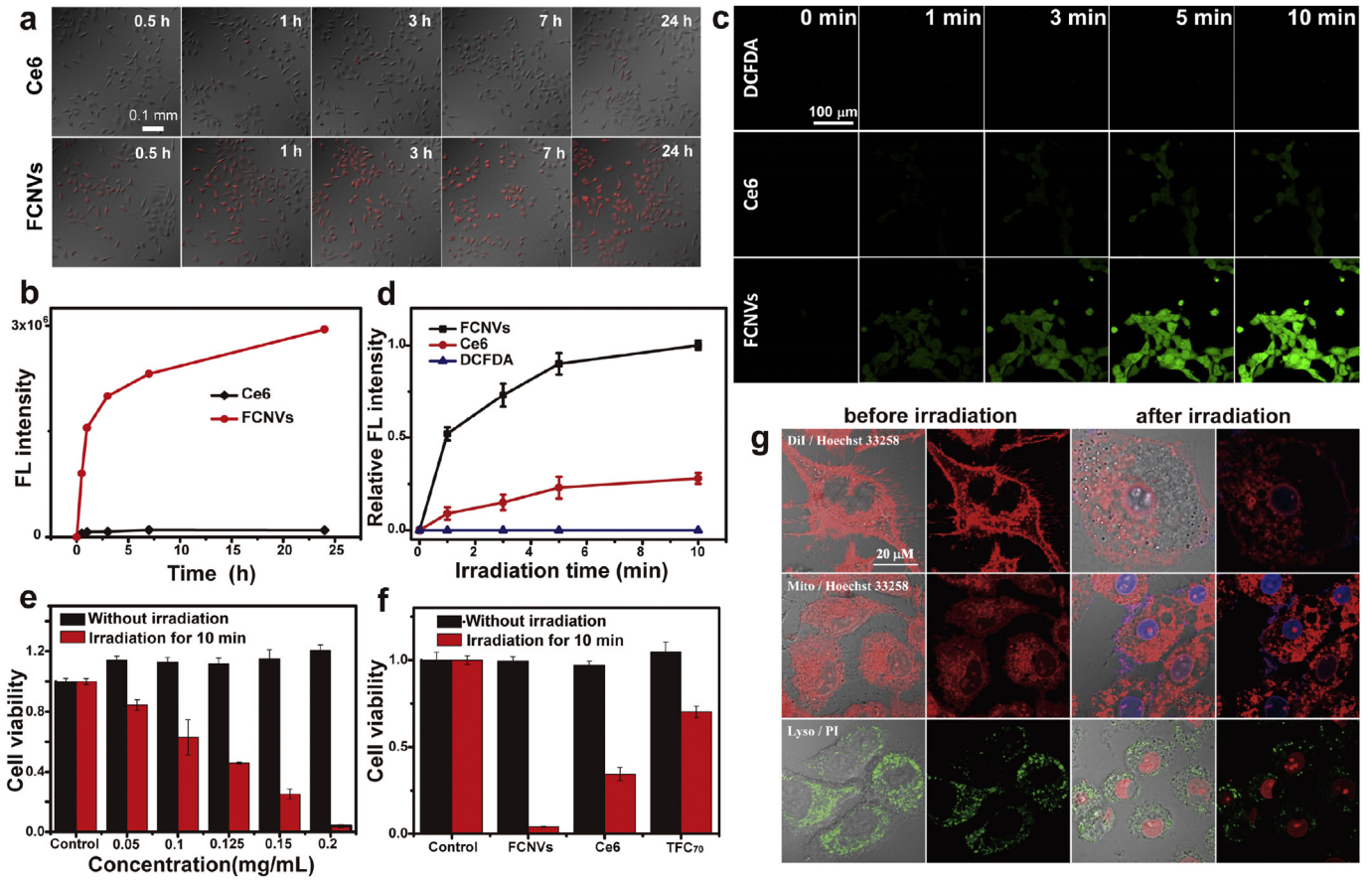

Fig. 3. (a) Confocal FL images of cells incubated with free Ce6 (above), and FCNVs (bottom) at different periods of incubation time (0.5, 1, 3, 7, and 24 h) at an equiv. Ce6 dose of 0.1 mg mL^{-1}. (b) Quantitative evaluation of the cellular uptake of Ce6 and FCNVs was carried out by comparing the FL intensities of cellular lysates at different incubation time. (c) Confocal images of DCFDA stained cells, and those subsequently treated with Ce6, and FCNVs at different irradiation time. (d) Time-dependent FL intensity of $^1O_2$ production detected by FL of DCFDA in A549 cells treated with Ce6, and FCNVs, respectively. Free DCFDA is used as control. (e) *In vitro* relative viabilities of A549 cells incubated with FCNVs at a gradient of concentrations, with 660 nm laser irradiation (red) or in dark (black). (f) Relative viabilities of A549 cells incubated with either FCNVs, or free Ce6 (at an equiv. Ce6 dose of 0.1 mg mL^{-1}) and TFC_{70} alone (0.1 mg mL^{-1}), respectively, with 660 nm laser irradiation (red) or in dark (black). (g) Confocal images before (left) and after 660 nm laser irradiation (right). First line was stained with DiI and Hoechst 33258, second line was stained with MitoRed and Hoechst 33258, third line was stained with PI and Lyso. Each group with two columns represents FL image and merged image, respectively.

irradiation with 660 nm laser. As shown in Fig. 3g, the images in the first row were stained by DiI (cell membrane dye) and Hoechst 33258 (nucleus dye), from which we can see clearly that the cell membrane was bubbling and the nuclei were stained with blue, suggesting that the cells were dead. The second row was stained by MitoRed tracker (mitochondrial dye) and Hoechst 33258, and the third row was stained by Lyso tracker (lysosome dye) and PI (nucleus dye). The compact mitochondria and lysosomes became incomplete and nuclei were stained with red and blue respectively after irradiation of 660 nm laser, indicating the subcellular organelles were destroyed by $^1O_2$ generated from FCNVs. In addition, two short videos were recorded for observing the changes of membrane (stained by DiI) and mitochondrial (stained by MitoRed) upon 660 nm laser irradiation in SI (MV), which clearly demonstrate the above phenomenon.

Supplementary video related to this article can be found at http://dx.doi.org/10.1016/j.biomaterials.2016.06.023

3.3. *In vivo* imaging and PDT

FL intensity of FCNVs *in vivo* was detected to evaluate the real-time biodistribution. For FL imaging studies, the luciferase-expressing breast cancer cell line (4T1-*luc*) was selected as the xenograft model and the tumor-bearing female Balb/c mice were injected with FCNVs through the tail vein (10 mg kg^{-1}). As expected, the FL images with negligible interference by autofluorescence from biological tissues could be used to monitor the biodistribution of FCNVs *in vivo*. As shown in Fig. 4a, a rapid tropism biodistribution associated with FCNVs accumulation was detected and the FL intensity of FCNVs in tumor significantly increased to the maximum after 4 h post-injection (top line). By contrast, the female Balb/c mouse treated with free Ce6 showed negligible FL in tumor site under the same conditions (bottom line), which is similar to the previous reports [61,73]. A sharp contrast of FCNVs *vs.* Ce6 treated mice could be seen from the chronologically statistical analysis of the relative average FL intensity at tumor site, as shown in Fig. 4b, further suggesting the significantly higher accumulation of the FCNVs than that of free Ce6 in tumor site. This result would facilitate the efficient PDT subsequently.

To evaluate the tumor inhibition efficacy of FCNVs under 660 nm irradiation *in vivo*, four groups (n = 5) of 4T1-*luc* tumor-bearing female Balb/c mice were used in our experiments. Under the guidance of FL imaging, the PDT treatment was conducted at 4 h post *i.v.* injection. The mice in the PDT treatment groups were intravenously injected with FCNVs (10 mg kg^{-1}) and then irradiated with 660 nm laser at power density of 100 mW cm^{-2} for

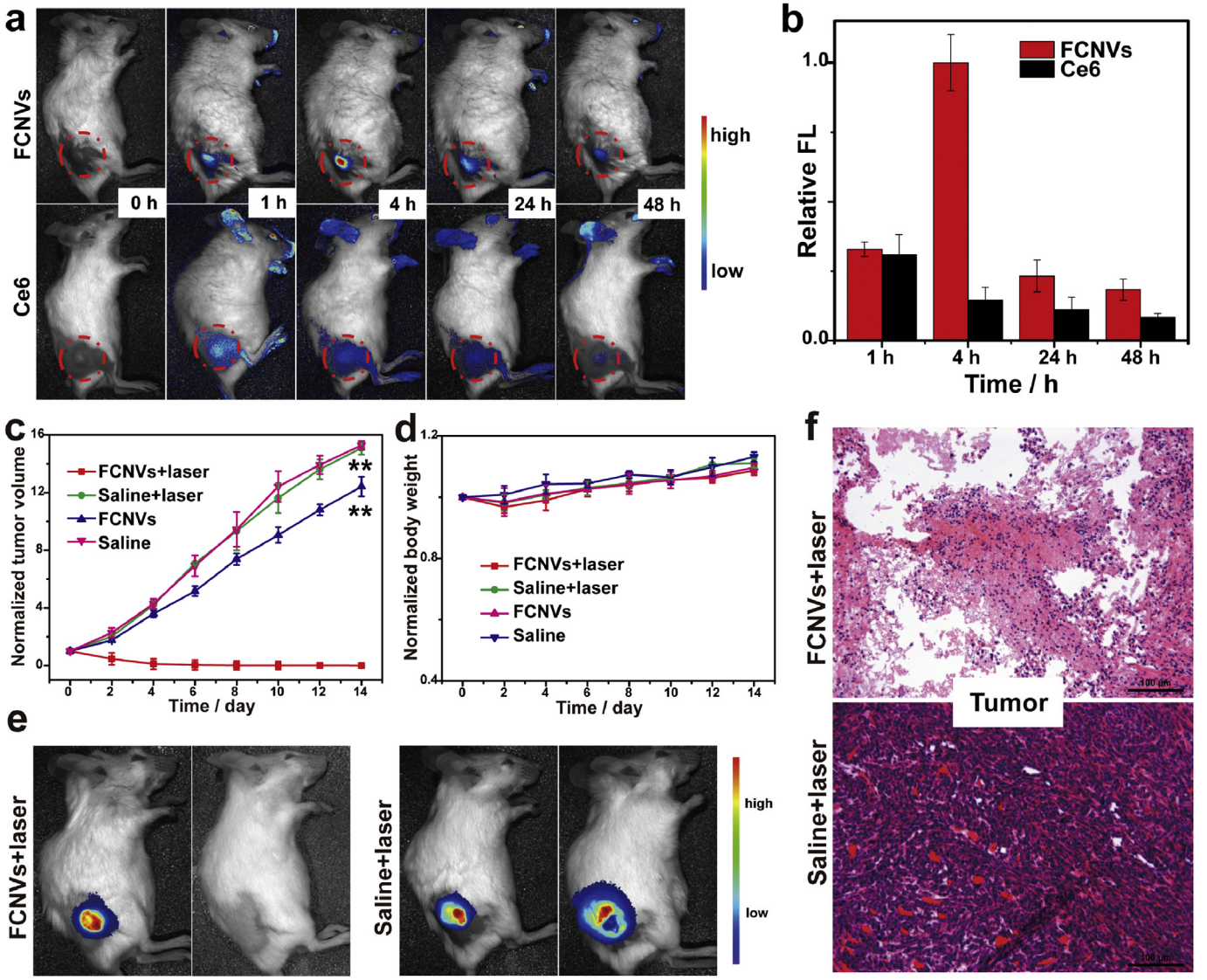

Fig. 4. (a) *In vivo* FL images of tumor-bearing mice at different time points after treatment with FCNVs (above) and Ce6 (bottom), respectively. (b) Relative FL intensity from tumor site at different time points for different treatments. (c) The relative tumor volumes were normalized to their initial sizes for three groups after different treatments. (d) The relative body weights of the Balb/c mice increased continuously after different treatments. Error bars indicate standard deviations; n = 5. (e) Bioluminescence images of before (left) and after treatment for 15 days (right). (f) H&E stained images of tumors under different PDT treatment.

10 min. In contrast, the mice administered with FCNVs or saline but not irradiated with laser, and mice treated with saline solution and subjected to laser irradiation were selected as control groups. The tumor sizes and weights of mice were monitored every second day. As shown in Fig. 4c, only the tumor of the mice treated with FCNVs and subsequently irradiated with 660 nm laser became black and scabby after 7 days treatment (Fig. S17†) and ablated after 15 days treatment, while the tumors in other three control groups continued growing along with time. In addition, body weight as an important parameter to roughly evaluate the toxicity of nanomedicine is monitored. As shown in Fig. 4d, no abnormal changes were found for all groups, indicating there is no obvious acute toxicity. The representative bioluminescence images of mice injected with FCNVs and subsequently exposed to 660 nm irradiation (Fig. 4e) were collected. The result reveals that the bioluminescence of experimental group nearly disappeared compared with saline-treated mice, which suggested that the tumor is effectively destroyed. Furthermore, H&E staining image of the tumor after PDT treatment shows obvious damage (Fig. 4f).

3.4. Biodistribution and clearance of FCNVs

To study whether or not the FCNVs can be cleared out from the body, 4T1-*luc* bearing Balb/c mice were sacrificed post-injection at 1 h, 4 h, 24 h, 2 d, 7 d, 15 d, and 20 d, respectively. Major organs (heart, liver, spleen, lung, kidneys, and muscle) and tumors were excised and imaged more accurately to evaluate the FL intensities within tissues. Mice injected with Ce6 were used as controls. Notably, strong FL from tumor, liver and kidney was detected, whereas negligible FL was observed in spleen, lung, muscle and heart, suggesting the FCNVs accumulate preferentially in former tissues, as shown in Fig. 5a and b. The average FL intensity of FCNVs accumulated in the tumor and organs areas quickly increases within 1–4 h post-injection, and decreases at 24 h. At 20 days post-injection, the FL decreases to undetectable level, which may excrete through the feces and urine due to their preferential accumulation

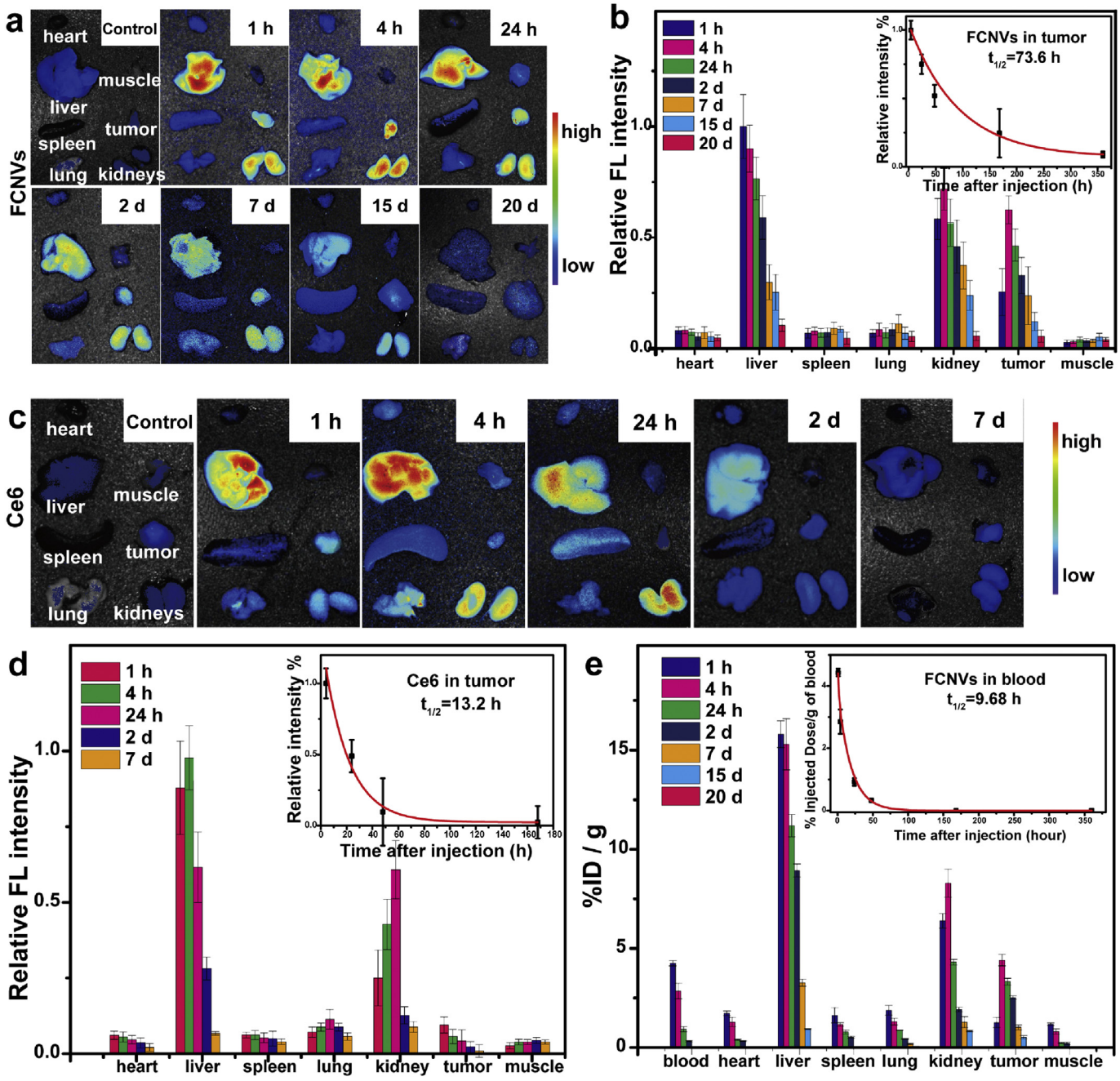

Fig. 5. (a) *Ex vivo* FL images of tumor and major organs after different time points post-injection of FCNVs. (b) Relative FL intensity of tumor and major organs after different time points post-injection of FCNVs. Inset is the measurement of half-life time ($t_{1/2}$) of FCNVs in tumor. (c) *Ex vivo* FL images of tumor and major organs after different time points post-injection of Ce6. (d) Relative FL intensity of tumor and major organs after different time points post-injection of Ce6. Inset is the measurement of half-life time ($t_{1/2}$) of Ce6 in tumor. (e) Biodistribution (%ID per g) at various time points post i.v. administration of ^{131}I-FCNVs. Inset is the measurement of half-life time ($t_{1/2}$) of FCNVs in bloodstream.

in liver and kidney [24,74]. In contrast, the *ex vivo* FL intensity of mice injected with free Ce6 mainly accumulated in liver and kidneys, and only a little accumulated in tumor site (Fig. 5c and d), which may ascribe to the low solubility and aggregating in water. Further investigation revealed the half-life ($t_{1/2}$) of FCNVs and Ce6 in tumor was 73.6 h and 13.2 h (Inset of Fig. 5b and d), respectively, indicating the blood circulation time of FCNVs was significantly longer than that of free Ce6 [75]. The biodistribution of FCNVs *in vivo* is difficult to be quantified accurately from FL measurement due to the tissue autofluorescence [76]. Therefore, the radiolabeling strategy [77–79] is demonstrated by incorporating radionuclides (^{131}I) into FCNVs, and the uptake (%ID per g) values of ^{131}I-FCNVs in bloodstream and major organs collected from Balb/c mice at different time points post tail vein injection (1 h, 4 h, 24 h, 2 d, 7 d, 15 d, and 20 d; n = 5 per time point) are plotted (Fig. 5e). The biodistribution and clearance of FCNVs in major organs and tumor are comparable to the FL measurement. At 20 days post-injection, the radio activity decreases to undetectable level, further confirming the complete clearance of FCNVs from the body. The half-life time of ^{131}I-FCNVs in bloodstream is 9.68 h (Insert of Fig. 5e), which is three times larger than that of previously reported free Ce6 (3.6 h) [74], due to the presence of OEG and the nanovesicular

structure of FCNVs [56,80,81]. H&E staining images of major organs are presented in Fig. S18†, the results don't show any obvious lesions, indicating FCNVs don't have significant toxicity to organism. The above results suggest that the FCNVs indeed could be excreted by liver and kidney with long time blood circulation and hold great promise for medical applications in cancer therapy.

4. Conclusion

In summary, we developed a novel phototheranostic platform based on FCNVs. Combining the respective advantages of fullerene and Ce6, the obtained FCNVs have the following characteristics: (i) a high Ce6 loading efficiency (up to ~57 wt%); (ii) efficient absorption in NIR region; (iii) enhanced cellular uptake efficiency *in vitro* as well as *in vivo*; (iv) simultaneous enhanced tumor imaging and PDT; (v) good biocompatibility and total clearance out from body. These unique properties suggest that as-prepared FCNVs can be used as new NIR-triggered phototheranostic agents for enhanced FL imaging guided PDT treatment. This work may pave the way for highly efficient phototheranostic applications based on FCNVs.

Acknowledgements

This work is supported by the National Natural Science Foundation of China (Nos. 51372251, 51472252) and the Key Research Program of the Chinese Academy of Sciences (Grant no. XDA09030302, KGZDEW-T02).

Appendix A. Supplementary data

Supplementary data related to this article can be found at http://dx.doi.org/10.1016/j.biomaterials.2016.06.023.

References

[1] X. Chen, S.S. Gambhir, J. Cheon, Theranostic nanomedicine, Acc. Chem. Res. 44 (2011) 841.
[2] K.K. Ng, G. Zheng, Molecular interactions in organic nanoparticles for phototheranostic applications, Chem. Rev. 115 (2015) 11012–11042.
[3] X. Yan, G. Niu, J. Lin, A.J. Jin, H. Hu, Y. Tang, Y. Zhang, A. Wu, J. Lu, S. Zhang, P. Huang, B. Shen, X. Chen, Enhanced fluorescence imaging guided photodynamic therapy of sinoporphyrin sodium loaded graphene oxide, Biomaterials 42 (2015) 94–102.
[4] Z. Gu, L. Yan, G. Tian, S. Li, Z. Chai, Y. Zhao, Recent advances in design and fabrication of upconversion nanoparticles and their safe theranostic applications, Adv. Mater. 25 (2013) 3758–3779.
[5] L. Wang, L.L. Li, Y.S. Fan, H. Wang, Host-guest supramolecular nanosystems for cancer diagnostics and therapeutics, Adv. Mater. 25 (2013) 3888–3898.
[6] D. Hu, Z. Sheng, G. Gao, F. Siu, C. Liu, Q. Wan, P. Gong, H. Zheng, Y. Ma, L. Cai, Activatable albumin-photosensitizer nanoassemblies for triple-modal imaging and thermal-modulated photodynamic therapy of cancer, Biomaterials 93 (2016) 10–19.
[7] J.P. Celli, B.Q. Spring, I. Rizvi, C.L. Evans, K.S. Samkoe, S. Verma, B.W. Pogue, T. Hasan, Imaging and photodynamic therapy: mechanisms, monitoring, and optimization, Chem. Rev. 110 (2010) 2795–2838.
[8] M. Guo, H. Mao, Y. Li, A. Zhu, H. He, H. Yang, Y. Wang, X. Tian, C. Ge, Q. Peng, X. Wang, X. Yang, X. Chen, G. Liu, H. Chen, Dual imaging-guided photothermal/photodynamic therapy using micelles, Biomaterials 35 (2014) 4656–4666.
[9] M. Ethirajan, Y. Chen, P. Joshi, R.K. Pandey, The role of porphyrin chemistry in tumor imaging and photodynamic therapy, Chem. Soc. Rev. 40 (2011) 340–362.
[10] X. Liang, X. Li, X. Yue, Z. Dai, Conjugation of porphyrin to nanohybrid cerasomes for photodynamic diagnosis and therapy of cancer, Angew. Chem. Int. Ed. 50 (2011) 11622–11627.
[11] J.F. Lovell, T.W. Liu, J. Chen, G. Zheng, Activatable photosensitizers for imaging and therapy, Chem. Rev. 110 (2010) 2839–2857.
[12] J. Ge, M. Lan, B. Zhou, W. Liu, L. Guo, H. Wang, Q. Jia, G. Niu, X. Huang, H. Zhou, X. Meng, P. Wang, C.S. Lee, W. Zhang, X. Han, A graphene quantum dot photodynamic therapy agent with high singlet oxygen generation, Nat. Commun. 5 (2014) 4596.
[13] J. Ge, Q. Jia, W. Liu, L. Guo, Q. Liu, M. Lan, H. Zhang, X. Meng, P. Wang, Red-emissive carbon dots for fluorescent, photoacoustic, and thermal theranostics in living mice, Adv. Mater. 27 (2015) 4169–4177.
[14] Z. Li, C. Wang, L. Cheng, H. Gong, S. Yin, Q. Gong, Y. Li, Z. Liu, PEG-functionalized iron oxide nanoclusters loaded with chlorin e6 for targeted, NIR light induced, photodynamic therapy, Biomaterials 34 (2013) 9160–9170.
[15] C. Wang, L. Cheng, Y. Liu, X. Wang, X. Ma, Z. Deng, Y. Li, Z. Liu, Imaging-guided pH-sensitive photodynamic therapy using charge reversible upconversion nanoparticles under near-infrared light, Adv. Funct. Mater. 23 (2013) 3077–3086.
[16] J. Lin, S. Wang, P. Huang, Z. Wang, S. Chen, G. Niu, W. Li, J. He, D. Cui, G. Lu, X. Chen, Z. Nie, Photosensitizer-loaded gold vesicles with strong plasmonic coupling effect for imaging-guided photothermal/photodynamic therapy, ACS Nano 7 (2013) 5320–5329.
[17] K. Liu, Y. Liu, Y. Yao, H. Yuan, S. Wang, Z. Wang, X. Zhang, Supramolecular photosensitizers with enhanced antibacterial efficiency, Angew. Chem. Int. Ed. 52 (2013) 8285–8289.
[18] Y. Huang, S. He, W. Cao, K. Cai, X. Liang, Biomedical nanomaterials for imaging-guided cancer therapy, Nanoscale 4 (2012) 6135–6149.
[19] J. Shi, X. Yu, L. Wang, Y. Liu, J. Gao, J. Zhang, R. Ma, R. Liu, Z. Zhang, PEGylated fullerene/iron oxide nanocomposites for photodynamic therapy, targeted drug delivery and MR imaging, Biomaterials 34 (2013) 9666–9677.
[20] M. Guan, T. Qin, J. Ge, M. Zhen, W. Xu, D. Chen, S. Li, C. Wang, H. Su, C. Shu, Amphiphilic trismethylpyridylporphyrin-fullerene (C_{70}) dyad: an efficient photosensitizer under hypoxia conditions, J. Mater. Chem. B 3 (2015) 776–783.
[21] M. Guan, H. Dong, J. Ge, D. Chen, L. Sun, S. Li, C. Wang, C. Yan, P. Wang, C. Shu, Multifunctional upconversion–nanoparticles–trismethylpyridylporphyrin–fullerene nanocomposite: a near-infrared light-triggered theranostic platform for imaging-guided photodynamic therapy, NPG Asia Mater. 7 (2015) e205.
[22] J. Shi, L. Wang, J. Gao, Y. Liu, J. Zhang, R. Ma, R. Liu, Z. Zhang, A fullerene-based multi-functional nanoplatform for cancer theranostic applications, Biomaterials 35 (2014), 5771–5584.
[23] L. Cheng, C. Wang, L. Feng, K. Yang, Z. Liu, Functional nanomaterials for phototherapies of cancer, Chem. Rev. 114 (2014) 10869–10906.
[24] Z. Chen, L. Ma, Y. Liu, C. Chen, Applications of functionalized fullerenes in tumor theranostics, Therasnostics 2 (2012) 238–250.
[25] G. Hong, S. Diao, A.L. Antaris, H. Dai, Carbon nanomaterials for biological imaging and nanomedicinal therapy, Chem. Rev. 115 (2015) 10816–10906.
[26] N. Gharbi, M. Pressac, M. Hadchouel, H. Szwarc, S.R. Wilson, F. Moussa, [60] fullerene is a powerful antioxidant in vivo with no acute or subacute toxicity, Nano Lett. 5 (2005) 2578–2585.
[27] Z. Li, J.C. Barnes, A. Bosoy, J.F. Stoddart, J.I. Zink, Mesoporous silica nanoparticles in biomedical applications, Chem. Soc. Rev. 41 (2012) 2590–2605.
[28] M.P. Melancon, M. Zhou, C. Li, Cancer theranostics with near-infrared light-activatable multimodal nanoparticles, Acc. Chem. Res. 44 (2011) 947–956.
[29] Z. Guo, S. Park, J. Yoon, I. Shin, Recent progress in the development of near-infrared fluorescent probes for bioimaging applications, Chem. Soc. Rev. 43 (2014) 16–29.
[30] L. Yuan, W. Lin, K. Zheng, L. He, W. Huang, Far-red to near infrared analyte-responsive fluorescent probes based on organic fluorophore platforms for fluorescence imaging, Chem. Soc. Rev. 42 (2013) 622–661.
[31] J. Bartelmess, S.J. Quinn, S. Giordani, Carbon nanomaterials: multi-functional agents for biomedical fluorescence and Raman imaging, Chem. Soc. Rev. 44 (2015) 4672–4698.
[32] V. Shanmugam, S. Selvakumar, C.S. Yeh, Near-infrared light-responsive nanomaterials in cancer therapeutics, Chem. Soc. Rev. 43 (2014) 6254–6287.
[33] E.K. Lim, T. Kim, S. Paik, S. Haam, Y.M. Huh, K. Lee, Nanomaterials for theranostics: recent advances and future challenges, Chem. Rev. 115 (2015) 327–394.
[34] J. Yao, M. Yang, Y. Duan, Chemistry, biology, and medicine of fluorescent nanomaterials and related systems: new insights into biosensing, bioimaging, genomics, diagnostics, and therapy, Chem. Rev. 114 (2014) 6130–6178.
[35] S.S. Babu, H. Möhwald, T. Nakanishi, Recent progress in morphology control of supramolecular fullerene assemblies and its applications, Chem. Soc. Rev. 39 (2010) 4021–4035.
[36] S. Zhou, C. Burger, B. Chu, M. Sawamura, N. Nagahama, M. Toganoh, U.E. Hackler, H. Isobe, E. Nakamura, Spherical bilayer vesicles of fullerene-based surfactants in water: a laser light scattering study, Science 291 (2001) 1944–1947.
[37] L. Zhang, Q. Feng, J. Wang, J. Sun, X. Shi, X. Jiang, Microfluidic synthesis of rigid nanovesicles for hydrophilic reagents delivery, Angew. Chem. Int. Ed. 54 (2015) 3952–3956.
[38] W. Jiang, Y. Zhou, D. Yan, Hyperbranched polymer vesicles: from self-assembly, characterization, mechanisms, and properties to applications, Chem. Soc. Rev. 44 (2015) 3874–3889.
[39] T. Bian, L. Shang, H. Yu, M.T. Perez, L.Z. Wu, C.H. Tung, Z. Nie, Z. Tang, T. Zhang, Spontaneous organization of inorganic nanoparticles into nanovesicles triggered by UV light, Adv. Mater. 26 (2014) 5613–5618.
[40] J. Song, P. Huang, H. Duan, X. Chen, Plasmonic vesicles of amphiphilic nanocrystals: optically active multifunctional platform for cancer diagnosis and therapy, Acc. Chem. Res. 48 (2015) 2506–2515.
[41] E. Huynh, B.Y. Leung, B.L. Helfield, M. Shakiba, J.A. Gandier, C.S. Jin, E.R. Master, B.C. Wilson, D.E. Goertz, G. Zheng, In situ conversion of porphyrin microbubbles to nanoparticles for multimodality imaging, Nat. Nanotechnol. 10 (2015) 325–332.

[42] Y. Li, T.Y. Lin, Y. Luo, Q. Liu, W. Xiao, W. Guo, D. Lac, H. Zhang, C. Feng, S. Wachsmann-Hogiu, J.H. Walton, S.R. Cherry, D.J. Rowland, D. Kukis, C. Pan, K.S. Lam, A smart and versatile theranostic nanomedicine platform based on nanoporphyrin, Nat. Commun. 5 (2014) 4712.
[43] R. Liang, S. You, L. Ma, C. Li, R. Tian, M. Wei, D. Yan, M. Yin, W. Yang, D.G. Evans, X. Duan, A supramolecular nanovehicle toward systematic, targeted cancer and tumor therapy, Chem. Sci. 6 (2015) 5511–5518.
[44] K. Baek, I. Hwang, I. Roy, D. Shetty, K. Kim, Self-assembly of nanostructured materials through irreversible covalent bond formation, Acc. Chem. Res. 48 (2015) 2221–2229.
[45] J.F. Lovell, C.S. Jin, E. Huynh, T.D. MacDonald, W. Cao, G. Zheng, Enzymatic regioselection for the synthesis and biodegradation of porphysome nanovesicles, Angew. Chem. Int. Ed. 51 (2012) 2429–2433.
[46] P. Huang, J. Lin, W. Li, P. Rong, Z. Wang, S. Wang, X. Wang, X. Sun, M. Aronova, G. Niu, Biodegradable gold nanovesicles with an ultrastrong plasmonic coupling effect for photoacoustic imaging and photothermal therapy, Angew. Chem. Int. Ed. 52 (2013) 13958–13964.
[47] J. Yoon, W. Jo, D. Jeong, J. Kim, H. Jeong, J. Park, Generation of nanovesicles with sliced cellular membrane fragments for exogenous material delivery, Biomaterials 59 (2015) 12–20.
[48] H. Sun, L. Miao, J. Li, S. Fu, G. An, C. Si, Z. Dong, Q. Luo, S. Yu, J. Xu, J. Liu, Self-assembly of cricoid proteins induced by “soft nanoparticles”: an approach to design multienzyme-cooperative antioxidative systems, ACS Nano 9 (2015) 5461–5469.
[49] X. Liang, B. Shi, K. Wang, M. Fan, D. Jiao, J. Ao, N. Song, C. Wang, J. Gu, Z. Li, Development of self-assembling peptide nanovesicle with bilayers for enhanced EGFR-targeted drug and gene delivery, Biomaterials 82 (2016) 194–207.
[50] Y. Tian, S. Li, J. Song, T. Ji, M. Zhu, G.J. Anderson, J. Wei, G. Nie, A doxorubicin delivery platform using engineered natural membrane vesicle exosomes for targeted tumor therapy, Biomaterials 35 (2014) 2383–2390.
[51] J. Song, L. Cheng, A. Liu, J. Yin, M. Kuang, H. Duan, Plasmonic vesicles of amphiphilic gold nanocrystals: self-assembly and external-stimuli-triggered destruction, J. Am. Chem. Soc. 133 (2011) 10760–10763.
[52] Q. Liu, M. Guan, L. Xu, C. Shu, C. Jin, J. Zheng, X. Fang, Y. Yang, C. Wang, Structural effect and mechanism of C70-carboxyfullerenes as efficient sensitizers against cancer cells, Small 8 (2012) 2070–2077.
[53] H. Tao, K. Yang, Z. Ma, J. Wan, Y. Zhang, Z. Kang, Z. Liu, In vivo NIR fluorescence imaging, biodistribution, and toxicology of photoluminescent carbon dots produced from carbon nanotubes and graphite, Small 8 (2012) 281–290.
[54] J. Fan, G. Fang, F. Zeng, X. Wang, S. Wu, Water-dispersible fullerene aggregates as a targeted anticancer prodrug with both chemo- and photodynamic therapeutic actions, Small 9 (2013) 613–621.
[55] R.J. Mart, K.P. Liem, X. Wang, S.J. Webb, The effect of receptor clustering on vesicle-vesicle adhesion, J. Am. Chem. Soc. 128 (2006) 14462–14463.
[56] K. Knop, R. Hoogenboom, D. Fischer, U.S. Schubert, Poly(ethylene glycol) in drug delivery: pros and cons as well as potential alternatives, Angew. Chem. Int. Ed. 49 (2010) 6288–6308.
[57] W. Nakanishi, K. Minami, L.K. Shrestha, Q. Ji, J.P. Hill, K. Ariga, Bioactive nanocarbon assemblies: nanoarchitectonics and applications, Nano Today 9 (2014) 378–397.
[58] Y. Liu, B. Liu, Z. Nie, Concurrent self-assembly of amphiphiles into nanoarchitectures with increasing complexity, Nano Today 10 (2015) 278–300.
[59] Y. Chang, K. Yang, P. Wei, S. Huang, Y. Pei, W. Zhao, Z. Pei, Cationic vesicles based on amphiphilic pillar[5]arene capped with ferrocenium: a redox-responsive system for drug/siRNA co-delivery, Angew. Chem. Int. Ed. 53 (2014) 13126–13130.
[60] J.P. Perdew, K. Burke, M. Ernzerhof, Generalized gradient approximation made simple, Phys. Rev. Lett. 77 (1996) 3865–3868.
[61] H. Park, K. Na, Conjugation of the photosensitizer chlorin e6 to pluronic F127 for enhanced cellular internalization for photodynamic therapy, Biomaterials 34 (2013) 6992–7000.
[62] P. Huang, C. Xu, J. Lin, C. Wang, X. Wang, C. Zhang, X. Zhou, S. Guo, D. Cui, Folic acid-conjugated graphene oxide loaded with photosensitizers for targeting photodynamic therapy, Theronatics 1 (2011) 240–250.
[63] M. Mahmoudi, I. Lynch, M.R. Ejtehadi, M.P. Monopoli, F.B. Bombelli, S. Laurent, Protein nanoparticle interactions: opportunities and challenges, Chem. Rev. 111 (2011) 5610–5637.
[64] S. Shen, F. Kong, X. Guo, L. Wu, H. Shen, M. Xie, X. Wang, Y. Jin, Y. Ge, CMCTS stabilized Fe3O4 particles with extremely low toxicity as highly efficient near-infrared photothermal agents for in vivo tumor ablation, Nanoscale 5 (2013) 8056–8066.
[65] F.M. Kievit, M. Zhang, Cancer nanotheranostics: improving imaging and therapy by targeted delivery across biological barriers, Adv. Mater 23 (2011) H217–H247.
[66] P. Huang, J. Lin, S. Wang, Z. Zhou, Z. Li, Z. Wang, C. Zhang, X. Yue, G. Niu, M. Yang, D. Cui, X. Chen, Photosensitizer-conjugated silica-coated gold nanoclusters for fluorescence imaging-guided photodynamic therapy, Biomaterials 34 (2013) 4643–4654.
[67] B. Tian, C. Wang, S. Zhang, L. Feng, Z. Liu, Photothermally enhanced photodynamic therapy delivered by nano-graphene oxide, ACS Nano 5 (2011) 7000–7009.
[68] C. Wang, H. Tao, L. Cheng, Z. Liu, Near-infrared light induced in vivo photodynamic therapy of cancer based on upconversion nanoparticles, Biomaterials 32 (2011) 6145–6154.
[69] T. Liu, C. Wang, W. Cui, H. Gong, C. Liang, X. Shi, Z. Li, B. Sun, Z. Liu, Combined photothermal and photodynamic therapy delivered by PEGylated MoS2 nanosheets, Nanoscale 6 (2014) 11219–11225.
[70] S. Sharifi, S. Behzadi, S. Laurent, M.L. Forrest, P. Stroeve, M. Mahmoudi, Toxicity of nanomaterials, Chem. Soc. Rev. 41 (2012) 2323–2343.
[71] A. Punjabi, X. Wu, A. Tokatli-Apollon, M. El-Rifai, H. Lee, Y. Zhang, C. Wang, Z. Liu, E.M. Chan, C. Duan, G. Han, Amplifying the red-emission of upconverting nanoparticles for biocompatible clinically used prodrug-induced photodynamic therapy, ACS Nano 8 (2014) 10621–10630.
[72] D. Zhang, M. Wu, Y. Zeng, L. Wu, Q. Wang, X. Han, X. Liu, J. Liu, Chlorin e6 conjugated poly(dopamine) nanospheres as PDT/PTT dual-modal therapeutic agents for enhanced cancer therapy, ACS Appl. Mater. Interfaces 7 (2015) 8176–8187.
[73] W. Miao, G. Shim, S. Lee, S. Lee, Y.S. Choe, Y. Oh, Safety and tumor tissue accumulation of pegylated graphene oxide nanosheets for co-delivery of anticancer drug and photosensitizer, Biomaterials 34 (2013) 3402–3410.
[74] E.B. Ehlerding, F. Chen, W. Cai, Biodegradable and renal clearable inorganic nanoparticles, Adv. Sci. 3 (2016), http://dx.doi.org/10.1002/advs.201500223.
[75] F. Ding, H. Li, J. Wang, W. Tao, Y. Zhu, Y. Yu, X. Yang, Chlorin e6-encapsulated polyphosphoester based nanocarriers with viscous flow core for effective treatment of pancreatic cancer, ACS Appl. Mater. Interfaces 7 (2015) 18856–18865.
[76] M. Schipper, G. Iyer, A. Koh, Z. Cheng, Y. Ebenstein, A. Aharoni, S. Keren, L. Bentolila, J. Li, J. Rao, X. Chen, U. Banin, A. Wu, R. Sinclair, S. Weiss, S. Gambhir, Particle size, surface coating, and PEGylation influence the biodistribution of quantum dots in living mice, Small 5 (2009) 126–134.
[77] K. Yang, S. Zhang, G. Zhang, X. Sun, S. Lee, Z. Liu, Graphene in mice: ultrahigh in vivo tumor uptake and efficient photothermal therapy, Nano Lett. 10 (2010) 3318–3323.
[78] X. Huang, F. Zhang, L. Zhu, K. Choi, N. Guo, J. Guo, K. Tackett, P. Anilkumar, G. Liu, Q. Quan, H. Choi, G. Niu, Y. Sun, S. Lee, X. Chen, Effect of injection routes on the biodistribution, clearance, and tumor uptake of carbon dots, ACS Nano 7 (2013) 5684–5693.
[79] K. Yang, L. Feng, X. Shi, Z. Liu, Nano-graphene in biomedicine: theranostic applications, Chem. Soc. Rev. 42 (2013) 530–547.
[80] M. Cavadas, A. González-Fernández, R. Franco, Pathogen-mimetic stealth nanocarriers for drug delivery: a future possibility, Nanomedicine 7 (2011) 730–743.
[81] J. Song, X. Yang, O. Jacobson, P. Huang, X. Sun, L. Lin, X. Yan, G. Niu, Q. Ma, X. Chen, Ultrasmall gold nanorod vesicles with enhanced tumor accumulation and fast excretion from the body for cancer therapy, Adv. Mater 27 (2015) 4910–4917.